ACS OMEGA

Open Access

http://pubs.acs.org/journal/acsodf

Article

Mesoporous Cu-Doped Manganese Oxide Nano Straws for Photocatalytic Degradation of Hazardous Alizarin Red Dye

Muhammad Hamza, Ataf Ali Altaf,* Samia Kausar, Shahzad Murtaza, Amen Shahpal, Muhammad Hamayun, Muhammad Tayyab, Komal Rizwan, Hamza Shoukat, and Anum Maqsood

Cite This: *ACS Omega* 2023, 8, 35956−35963

Read Online

ACCESS | Metrics & More | Article Recommendations | Supporting Information

ABSTRACT: The present work reports the photocatalytic degradation of alizarin red (AR) using Cu-doped manganese oxide (**MH16−MH20**) nanomaterials as catalysts under UV light irradiation. Cu-doped manganese oxides were synthesized by a very facile hydrothermal approach and characterized by energy dispersive X-ray spectroscopy, powder X-ray diffraction, scanning electron microscopy, Brunauer−Emmett−Teller analysis, UV−vis spectroscopy, and photoluminescence techniques. The structural, morphological, and optical characterization revealed that the synthesized compounds are nanoparticles (38.20−54.10 nm), grown in high mesoporous density (constant $C > 100$), possessing a tetragonal phase, and exhibiting 2.98−3.02 eV band gap energies. Synthesized materials were utilized for photocatalytic AR dye degradation under UV light which was monitored by UV−visible spectroscopy and % AR degradation was calculated at various time intervals from absorption spectra. More than 60% AR degradation at various time intervals was obtained for **MH16−MH20** indicating their good catalytic efficiencies for AR removal. However, **MH20** was found to be the most efficient catalyst showing more than 84% degradation, hence **MH20** was used to investigate the effect of various catalytic doses, AR concentrations, and pH of the medium on degradation. More than 50% AR degradation was obtained for all studied parameters with **MH20** whereas the pseudo-first-order kinetic model was found to be the best-fitted kinetic model for AR degradation with $k = 0.0015$ and $R^2 = 0.99$ indicating a significant correlation between experimental data.

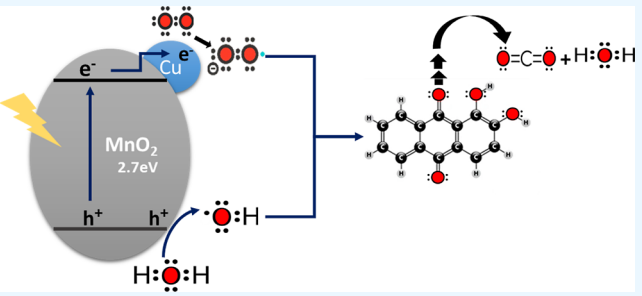

1. INTRODUCTION

Organic dyes belong to the class of synthetic organic compounds that are frequently used in textile, paper, pharmaceutical, and leather industries to color fabrics.[1] These dyes are often discharged into the environment after being used and washing operations. The textile, printing, papermaking, food processing, pharmaceutical, and cosmetics industries can all be potential sources of effluent containing substantial amounts of these organic dyes.[2] These dyes which are visible even in small traces pollute the water reservoirs and prove to be highly toxic, mutagenic, and carcinogenic.[3]

Most of these synthetic dyes used in various industries are generally very resistant to microbial- or bio-degradation.[4] Hence various methods and techniques like coagulation, adsorption, ion flotation, and sedimentation have been adopted until now to effectively remove these toxic dyes from water bodies.[5] However, these all techniques end up producing a large amount of secondary waste which requires attention to be processed further. To overcome these drawbacks, a lot of efforts have been made to develop sustainable strategies like oxidation catalysis or adsorption catalysis incorporating advanced oxidation processes[6] such as the Fenton process,[7] sonolysis, ozonation process, and UV photolysis to overcome common strategic barriers.[8]

Among these techniques, photocatalysis has gathered an enormous amount of interest owing to being a green technology that leads to the total mineralization of synthetic organic dyes into more degradable and less toxic substances with low initial and operating costs.[9] Photocatalytic degradation of dyes employed at ambient temperature and pressure conditions is considered environmentally friendly as it does not produce any polycyclic products.[10]

Alizarin red (AR) (1,2-dihydroxy-9,10-anthraquinone sulfonic acid sodium salt; AR; a water-soluble anthraquinone dye) has been widely used in the textile industries[11] and hence is a major textile effluent. A lot of work has been carried out on its degradation in an aqueous medium.[12] Different studies were carried out for photocatalytic AR degradation employing

Received: May 30, 2023
Accepted: August 31, 2023
Published: September 22, 2023

various catalysts. Joshi and co-workers employed ZnO and TiO_2-based photocatalysts for AR degradation under UV irradiation and got the highest degradation percentage after 3 h.[13] Kansal and co-workers[1c] have reported ZnO as a catalyst for the degradation of AR dye under UV irradiation and got 77% degradation after 90 min.

Various transition-metal oxides are being investigated as catalysts for organic dye degradation purposes using direct sunlight or UV light irradiation in recent reports.[14] Oxides like TiO_2,[11] ZnS, Cd-doped ZnS,[15] G-TiO_2 supported at Fe_3O_4,[16] and Ce-doped-Bi_2O_3[16] have been extensively used in the degradation of azo dyes.[17] However, manganese oxides with wide band gaps unique electrical, optoelectronic, and luminescence properties and large exciton-binding-energies have been proven promising and potential photocatalysts for photocatalytic degradation of various organic dyes. Various kinds of soft templates have been employed to increase surface areas, pore volumes, and stabilities of manganese oxide-based catalysts. However, doped with other transition metal materials have attracted much attention due to their role in the enhancement of catalytic efficiency of materials and copper has been reported as an important dopant material for manganese oxide nanomaterials.[11]

In this present study, photocatalytic degradation of AR was investigated under UV light irradiation using copper-doped manganese oxide nanomaterials (**MH16−MH20**) as catalysts. Doped/undoped manganese oxide nanomaterials are promising materials due to their low cost, high stability, and good environmental compatibility.[18] Nanomaterials were synthesized by a very facile hydrothermal method and used for the degradation of (AR) dye under UV irradiation. The effect of the time, various catalyst doses, different dye concentrations in the aqueous solutions, and pH of the dye solutions have been investigated.

2. MATERIALS AND METHODS

Chemical $KMnO_4$, $Cu(NO_3)_2$, HCl, and AR dye were purchased from Sigma-Aldrich. All the chemicals were of analytical grade and used without more purification.

Powder X-ray diffraction (PXRD) measurements were performed in an X-ray diffractometer (Bruker, AXS D8) with Cu-Kα radiation (1.5406 Å) at a scanning rate of 10 min in the 2θ range from 10 to 90°. Morphological features of catalysts were characterized by a scanning electron microscope (JEOL, JSM-6360 EO), and elemental composition was estimated by an energy-dispersive X-ray diffractometer (JEOL JSM-6360 LV). The surface area and pore structure parameters were calculated by Brunauer−Emmett−Teller (BET) analysis performed through Quantachrome Nova 2200e. UV spectra of the prepared nanomaterial was recorded by a UV3092 UV−vis spectrometer. The photoluminescence (PL) study was carried out with a spectrophotometer (Shimadzu) at an excitation wavelength of 420 nm. A sonicator (Bransonic 2510EMT bath) was used for surface area deployment of nanomaterials. PTFE-lined, stainless steel, Parr 5521 high-pressure compact autoclave was used for temperature and pressure treatment. A UV lamp (length: 288 mm, pipe diameter: 16 mm, voltage: 220 V, power; 8 W, wavelength range: 240−285 nm) was used as a light source for photocatalytic AR dye degradation activity. Catalytic dye degradation was studied by a UV spectrophotometer (Shimadzu) in the frequency range of 250−800 nm.

2.1. Synthesis of Copper Manganese Oxide Nanomaterials (MH16−MH20). **MH16** was prepared hydrothermally by taking 0.948 g of $KMnO_4$ and 0.38 g of $Cu(NO_3)_2$ (in a ratio of 1:3) dissolved in 50 mL of water in an autoclave container. The reaction mixture was stirred for 30 min followed by the addition of 20 mL of HCl in the mixture. The entire mixture was heated at 180 °C for 24 h in the oven. After heat treatment, the autoclave cooled down to room temperature, and dark brown precipitates were separated. Precipitates were washed with distilled water at various times, dried, and powdered. **MH17−MH20** were prepared by following the same method as above by taking 0.42, 0.45, 0.48, and 0.50 g of $Cu(NO_3)_2$ for the synthesis of each, respectively. Synthesized series of compounds were characterized and investigated for catalytic studies.

2.2. Photocatalytic Degradation of AR. Photocatalytic degradation of AR dye catalysts was carried out using **MH16−MH20** as a catalyst following our earlier reported method.[19] For dye degradation activity, a 100 ppm solution of AR dye (0.1 g) was prepared in water. First of all, blank experiments were carried out using a dye solution without a catalyst. The blank 1 experiment was carried out without UV light irradiation and spectra were recorded at different time intervals. Blank 2 experiment was done by irradiating the dye solution and UV spectra were taken at different time intervals by taking sample aliquots.

Photocatalytic degradation of AR dye was carried out in the presence of synthesized nanomaterials **MH16−MH20** as catalysts to investigate their catalytic efficiencies. For activity, 50 mL of 200 ppm AR dye (0.2 g) solution was taken in a flask and stirred under a UV light source in the presence of 0.02 g of **MH16**. Sample aliquots of 5 mL were taken out from the reaction mixture after 30, 60, 90, 120, 150, and 180 min. All the sample aliquots taken at various time intervals were centrifuged to separate the catalyst and the UV spectrum was recorded. Absorbance at 501 nm was noted from the individual spectra of each aliquot and the percentage degradation of AR dye was calculated through eq 1.[20]

$$\% \text{ Degradation} = 1 - \frac{C_t}{C_0} \times 100 \quad (1)$$

where C_0 is the initial concentration and C_t is the concentration at certain time intervals at which sample aliquot is taken. The concentration of AR after reaction time was calculated by the calibration curve between the absorbance and known AR concentration. The same method was adopted to perform the catalytic activity for all other catalysts **MH17−MH20**.

The percent degradation of AR dye was calculated by variating the initial dye concentration as 50, 100, 150, 200, and 250 ppm, variating catalyst dose as 0.015, 0.02, 0.025, 0.03, 0.035, and 0.040 g, and pH of AR dye solution from 3−11. Each experiment was performed following the method described above. The pH was adjusted by using HCl for acidic pH and NaOH for the basic medium.

3. RESULTS AND DISCUSSION

3.1. Characterization of Nanomaterials (MH16−MH20). *3.1.1. Elemental Analysis by EDX.* The elemental analysis of all the synthesized materials (**MH16−MH20**) was carried out by the EDX analysis technique and the elemental composition found in this respect is reported in Table 1. The

https://doi.org/10.1021/acsomega.3c03736
ACS Omega 2023, 8, 35956−35963

Table 1. Synthetic Conditions, PXRD Parameters, and Composition of Nanomaterials (MH16−MH20)

sample codes	synthetic conditions	unit formula and composition by EDX	average crystallite size D (nm)	volume $V = D^3$	dislocation density (δ) $(nm)^{-2}$	microstrain (ε)
MH16	0.95 g of KMnO4, 0.38 g $Cu(NO_3)2$ and HCl	$(Mn_{0.88}Cu_{0.15}O_2)$, Mn (55.39); Cu (10.09); O (36.52)	46.25 ± 4	43,562	3.44×10^{-4}	0.018
MH17	0.95 g of KMnO4, 0.42 g $Cu(NO_3)2$ and HCl	$(Mn_{0.80}Cu_{0.22}O_2)$, Mn (51.28); Cu (9.12); O (39.51)	39.22 ± 3	48,756	3.87×10^{-4}	0.022
MH18	0.95 g of KMnO4, 0.45 g $Cu(NO_3)2$ and HCl	$(Mn_{0.80}Cu_{0.23}O_2)$, Mn (51.89); Cu (9.21); O (38.90)	38.20 ± 5	66,548	4.66×10^{-4}	0.042
MH19	0.95 g of KMnO4, 0.48 g $Cu(NO_3)2$ and HCl	$(Mn_{0.82}Cu_{0.25}O_2)$, Mn (53.28); Cu (9.46); O (37.26)	48.65 ± 3	86,451	3.23×10^{-4}	0.038
MH20	0.948 g of KMnO4, 0.41 g $Cu(NO_3)2$ and HCl	$(Mn_{0.80}Cu_{0.23}O_2)$, Mn (50.89); Cu (9.18); O (39.93)	54.10 ± 5	88,265	4.78×10^{-4}	0.047

results in Table 1 for nanomaterials (**MH16−MH20**) indicated that the analyzed elemental compositions are in close agreement with the reactants used for synthesis. Mn was present as the major phase with percentage elemental composition ranges from 50.89 to 55.39% whereas Cr was found as a minor phase with percentage composition ranges of 9.12−10.09%.

3.1.2. PXRD Analysis. Synthesized catalysts **MH16−MH20** were analyzed by the PXRD technique and the data obtained is reported in Table 1. PXRD patterns of **MH16−MH20** are presented in Figure 1. Synthesized nanomaterials have shown

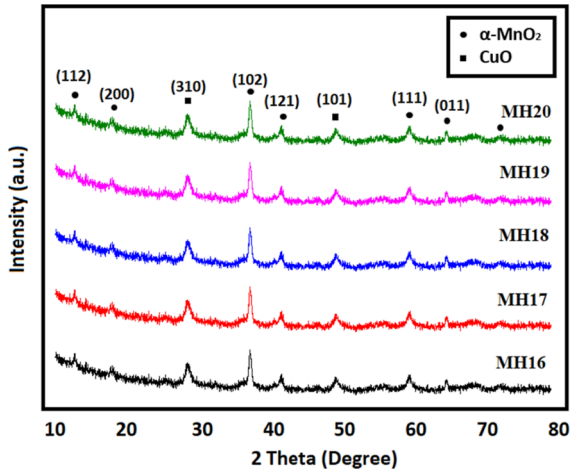

Figure 1. PXRD patterns of nanomaterials (**MH16−MH20**).

peak intensities at 2θ values corresponding to lattice planes, i.e., 11.04 (112), 19.43(200), 28.10(310), 41.83(121), 49.79(101), 59.54(111), 64.20(112), and 71.33(112) in PXRD patterns that were matched with literature-reported standard powder patterns of α-MnO_2 (JCPD no. 80-1098, 01-1127)[21] and CuO (JCPD no. 21-0269, 70-3766).[22] PXRD patterns of MH16−MH20 depicted that α-MnO_2 was present as the major phase and CuO as the minor phase (marked in Figure 1) which is in accordance with their elemental composition obtained through EDX. Peaks for α-MnO_2 have shown a gradual decrease in intensity from **MH16** to **MH20** and an increase in intensity was observed for CuO. The major phase α-MnO_2 was found to be tetragonal in structure having the $P\bar{4}2/mnm$ space group. PXRD parameters and elemental composition are given in Table 1.

After phase determination in synthesized materials, PXRD parameters like crystallite size (D), dislocation density (δ), crystallite volume (V), and microstrain (ε) were calculated for all and are reported in Table 1. Particle size was calculated employing the Debye Scherrer formula ($D = 0.91\lambda/\beta \cos\theta$).[23] The volume ($V$) of crystalline is determined using the equation ($V = D^3$).[24] The number of defects in the samples was measured as dislocation density ($\delta = 1/D^2$).[25] Crystal broadening and distortions were calculated as microstrain ($\varepsilon = \beta/4 \tan\theta$).[26] Positive and negative values of microstrain denote the tensile or compressive type of strain in samples.[26]

Average crystallite sizes for nanomaterials **MH16−MH20** at their corresponding intensities were calculated as 46.25, 39.22, 38.2, 48.65, and 54.10 nm, respectively. The crystallite size was observed to have increased as the concentration of Cu increased as reported in Table 1. The nanomaterials exhibited very small numbers for dislocation density indicating that the extent of detection was insignificant. The α-MnO_2 structure showed greater imperfection and strain as the concentration increased for Cu ions from **MH16** to **MH20**. Positive but very few values for microstrain were observed which is ascribed to the shrinkage in the lattice structures as the crystallite size and Cu ions' concentration increase.

3.1.3. Scanning Electron Microscopy Analysis. Surface morphological features were analyzed by SEM for all the synthesized nanomaterials **MH16−MH20** and SEM spectrographs are provided in Supporting Information, Figure S1. SEM images depicting straw type structure for representative compounds **MH16** and **MH17** are given in Figure 2 with WD

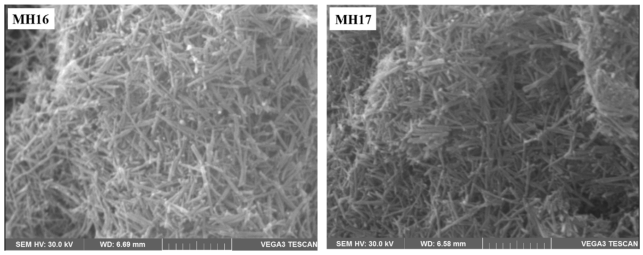

Figure 2. SEM images of representative nanomaterials (**MH16−MH17**).

= 6.69 and 6.58 nm for both, respectively. All the nanomaterials were in the same phase depicting homogeneous dispersity whereas their structural appearance resembles straw-like structures.

3.1.4. BET Analysis. The specific surface area of synthesized nanomaterials **MH16−MH20** was calculated by multipoint BET and pore structure parameters were calculated through the DFT method and are enlisted in Table 2. N_2 adsorption−desorption isotherms of representative sample MH16 is provided in Figure S2 of Supporting Information. The specific surface area of synthesized nanomaterials was in the range of 38−49 m^2/g. Material **MH17** has the maximum surface area,

https://doi.org/10.1021/acsomega.3c03736
ACS Omega 2023, 8, 35956−35963

Table 2. BET Properties of Synthesized Nanomaterials (MH16−MH20)

BET properties	samples				
	MH16	MH17	MH18	MH19	MH20
surface area (S_{BET}) (m^2/g)	41.22	49.03	39.221	48.02	38.21
pore volume (V_m) (cc/g)	0.022	0.009	0.011	0.033	0.029
pore width (nm)	2.997	3.331	3.112	2.113	4.245
constant	2298	6021	7790	1127	4427
Pore Structure Parameters					
cumulative surface area of pores (S_{DFT}) (m^2/g)	11.5	15.11	10.08	14.18	9.56
cumulative pore volume (V_{DFT}) (cc/g)	0.018	0.023	0.016	0.021	0.016
cumulative pore width (nm)	7.54	9.24	7.15	8.79	7.08

i.e., 49.03 m^2/g whereas **MH20** has 38.21 m^2/g. All the synthesized nanomaterials were found to be mesoporous as depicted by constant C values. These high values of C constant characterize the high content of porosity and strong adsorbent−adsorbate interactions between the catalyst surface and dye.

3.1.5. Optical Characterization. 3.1.5.1. UV−vis Spectral Analysis. To study the optical studies of synthesized nanomaterials, UV−vis was performed and Figure 3a depicts the UV−vis spectra of Cu-based manganese oxide nanomaterials **MH19** and **MH20**. The optical energy band gaps from absorptions were calculated through Tauc plots between energy and $(\alpha h\nu)$ i.e., $(\alpha h\nu) = A(h\nu - Eg)$[27] where A is the band edge parameter as shown in Figure 3a. Absorptions at 374 and 377 nm were observed for **MH19** and **MH20** which correspond to 3.02 and 2.98 eV band gap, respectively. The calculated band gap energies exhibit the potential of synthesized materials to absorb light in the UV−vis to visible region and their use as efficient photocatalytic applications.[28]

3.1.5.2. PL Study. PL emission spectra of the synthesized nanomaterials **MH17−MH20** were recorded at an exciton wavelength of 375 nm. These nanomaterials exhibited broad PL peaks in the visible region in the range from 410 to 470 nm as represented in Figure 3b. PL spectra of synthesized nanomaterials (**MH17−MH20**) were observed to be showing prominent emission peaks at 420, 430, and 445 nm corresponding to the 2.98 and 3.02 eV energy band gap which is usually associated with oxygen vacancy-related defects.[29] No peak shifting was observed in PL spectra which depicts that catalysts are devoid of strain in the distributed nanomaterial. Lower intensities show a lower recombination rate of photo-generated electron−hole owing to an increased Cu concentration in **MH17−MH20**. Low energies of charge recombination center enhance charge carrying capacities of nanomaterials and hence may play an important role in enhancing the catalytic efficiencies.

3.2. Photocatalytic Degradation of AR under UV Light by MH16−MH20. Photocatalytic degradation of AR dye was carried out under irradiation of UV light and samples were taken at different times. For all the aliquots taken, absorbance at 505 nm was recorded through a UV spectrophotometer and factors like the effect of time, catalytic dose, initial dye concentrations, and pH were investigated under UV light. Absorption spectra of all aliquots depicted a decrease in absorption intensities which may be ascribed to the decomposition of aromatic rings.

Absorption spectra were taken for AR degradation experiments carried out without catalysts under UV light irradiation as blank 1 and without UV light irradiation as blank 2. No change was observed in the spectrum of the blank 1 experiment indicating no degradation of AR whereas a slight change was detected in the absorption spectra of the blank 2 experiment carried out under UV light irradiation. Photocatalytic AR dye degradation using all synthesized nanomaterials (**MH16−MH20**) as catalysts was investigated and % degradation was calculated for each studied factor below.

3.2.1. AR Degradation with Increasing Time. To investigate the degradation of $AR_{200\ ppm}$ dye with increasing time intervals using 0.025 g of **MH16−MH20** as catalysts, absorption spectra were recorded for sample aliquots during photocatalytic experiments after 30, 60, 90, 120, 150, and 180 min as shown in Figure S3. The percent degradation was calculated for each time and data are enlisted in Table 3. **MH16−MH20** showed 39.89, 33.21, 32.61, 31.11, and 46.02%

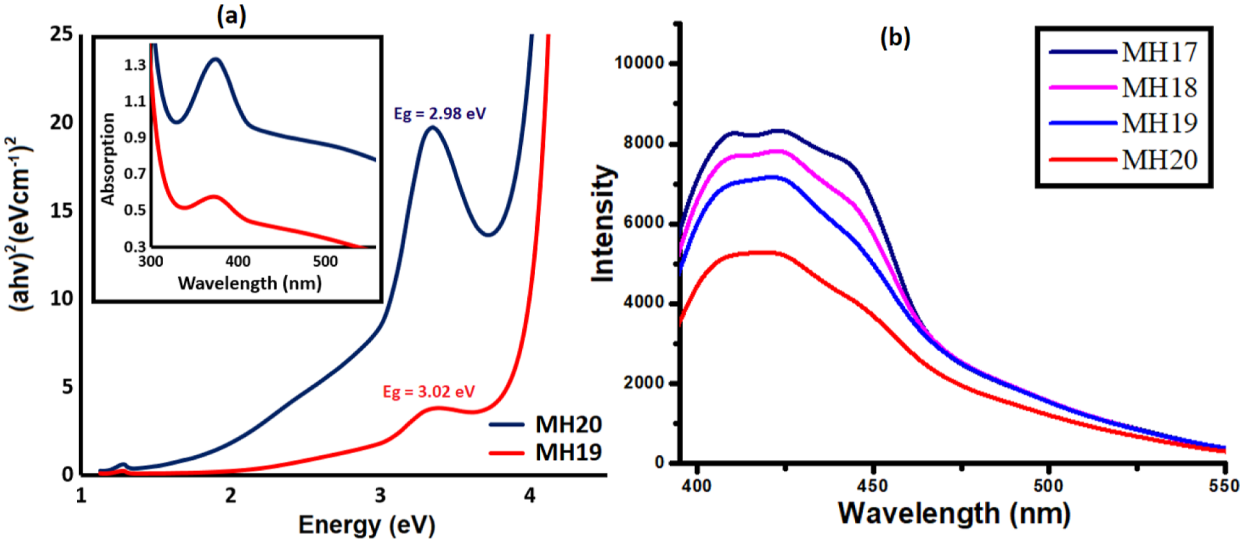

Figure 3. (a) Tauc plot for band gap energy and UV−vis spectra (inset) of representative nanomaterials **MH19** and **MH20**. (b) PL spectra of the photocatalysts (**MH17−MH20**).

https://doi.org/10.1021/acsomega.3c03736
ACS Omega 2023, 8, 35956−35963

Table 3. Percentage AR Degradation by MH16−MH20 with Increasing Time

time (min)	MH16	MH17	MH18	MH19	MH20
30	39.89	33.21	32.61	31.11	46.02
60	46.03	42.32	43.12	44.02	53.95
90	57.02	49.33	52.09	52.07	62.20
120	62.12	56.33	58.21	59.22	67.98
150	71.88	59.29	67.76	69.11	77.13
180	76.22	62.06	71.76	78.23	84.19

AR degradation, respectively, after 30 min of photocatalytic activity under UV light (Figure 4). An increase in % AR degradation was found to have increased with increasing catalyst dose from 0.020 to 0.040 g/L as shown in Figure 5.

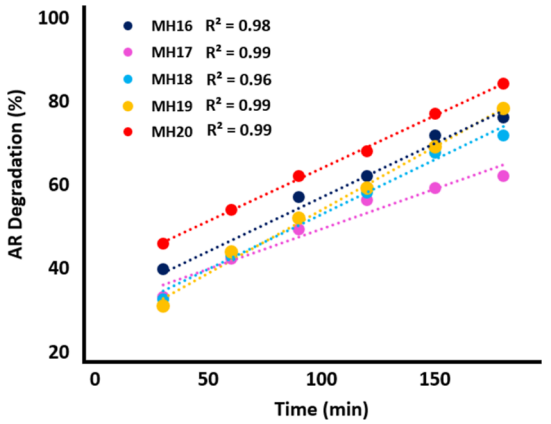

Figure 4. Photocatalytic $AR_{200\ ppm}$ degradation at different time intervals by 0.025 g of **MH1−MH5** as catalysts.

degradation was observed with every increasing time interval. For **MH16**, 43.48% AR degradation was calculated after 60 min which got increased to 76.22% after 180 min. Similarly, more than 42.32% degradation was observed for **MH17**and **MH18** after 60 min which got increased to 62.06 and 71.76%, respectively, after 180 min of catalytic activity. Among all the catalysts, **MH19** and **MH20** have shown maximum photocatalytic efficiencies after 60 min with 44.02 and 53.95% degradation percentages which got increased to 78.23 and 84.19%. The correlation between % AR degradation and time of the experiment was found to be significant as the R^2 value calculated were close to 1 for each activity experiment.

3.2.2. Effect of Increasing Catalyst Doses. **MH20** was found to be the most efficient catalyst as indicated by the degradation obtained under different time intervals as discussed in Section 3.2.1. Hence, different doses, i.e., 0.020, 0.025, 0.030, 0.035, and 0.040 g/L of **MH20** were employed to investigate the AR degradation after 60 min of photocatalytic treatment under UV light irradiation. Absorption spectra were recorded and % degradation was calculated for each catalytic dose which is enlisted in Table 4. The percentage of AR

Table 4. AR_{250ppm} Degradation by Various Catalytic Doses of MH20 after 60 min of Photocatalytic Activity

amounts (g)	% AR degradation
0.020	50.32
0.025	53.95
0.030	57.16
0.035	78.09
0.040	89.73

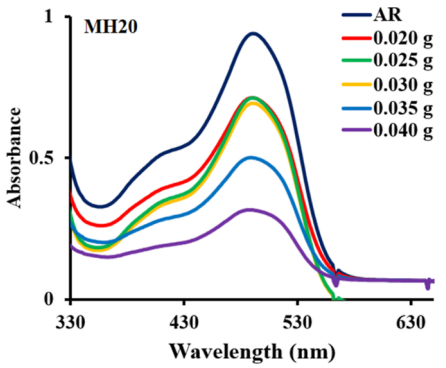

Figure 5. $AR_{200\ ppm}$ degradation with different catalyst doses of **MH20** after 60 min of photocatalytic activity.

Approximately, 50.32, 53.95, and 57.16% AR degradation percentage was calculated for 0.020, 0.025, and 0.030 g of **MH20**, respectively. However, increasing the dose above 0.030 g gave a notable increase in degradation of AR as 78.09 and 89.73% degradation was observed for 0.035 g and 0.040 g **MH16**, respectively. An increase in % AR degradation with an increase in dosage of **MH20** is possibly ascribed to the maximum surface area available of the catalyst resulting in more light photons reaching the surface.[21]

3.2.3. Effect of the Increasing Dye Concentration. The degradation efficiency of **MH20** was monitored by varying the concentrations of AR dye, i.e., 50, 100, 150, 200, and 250 ppm for 60 min of UV light. The amount of **MH20** used for each experiment was 0.020 g/L. The percentage was calculated from UV spectra (Figure 6) taken for each experiment and data are

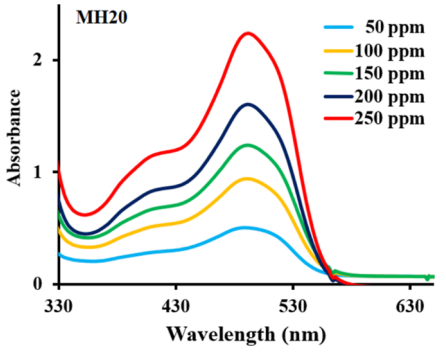

Figure 6. Degradation with different AR concentrations (50−250 ppm) by 0.020 g of **MH20** after 60 min of photocatalytic activity.

Table 5. Degradation of Different AR Concentrations (50−250 ppm) by 0.020 g of MH20 after 60 min of Photocatalytic Activity

dye concentration (ppm)	% AR degradation
50	83.24
100	71.20
150	62.04
200	50.32
250	49.13

https://doi.org/10.1021/acsomega.3c03736
ACS Omega 2023, 8, 35956−35963

enlisted in Table 5. The percentage of AR degradation was decreased for each increasing concentration of AR solution from 50 to 250 ppm. More than 80% dye degradation was observed when 50 ppm AR solution was subjected to degradation under UV light. Increasing the concentration of AR from 50 to 250 ppm degradation percent reduced to 71.20% with 100 ppm, 62.04% with 150 ppm, 50.32% with 200 ppm, and 49.13% with 250 ppm. This decline in degradation of AR at substrate concentrations is most possibly due to the adsorption of a greater number of AR molecules on the surface of the catalyst which resulted in fewer active sites available on the catalyst's surface. More number of AR molecules adsorbed on the catalyst surface made less number of light photons get to the surface ultimately resulting in decreased UV light available for the excitation of catalyst particles.[21]

3.2.4. Effect of pH of Medium. The effect of changing the pH of AR solution on its degradation was investigated by changing the solution pH from acidic (pH = 3, 5) to basic (pH = 9, 11). The 200 ppm solution of AR was used for each experiment for 60 min under UV light irradiation using 0.020 g of **MH20** as the catalyst and AR degradation was calculated (Figure 7). The percentage of AR degradation at pH = 7 was

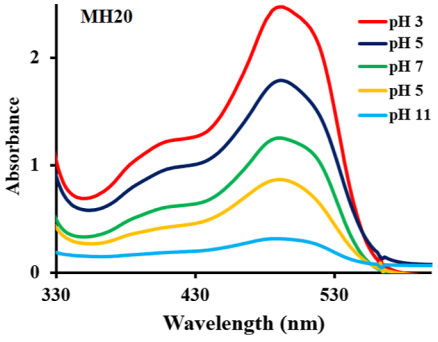

Figure 7. Degradation of $AR_{200\ ppm}$ by 0.020 g of **MH20** after 60 min of photocatalytic activity at various pH.

calculated as 50.32% which was increased when the pH of AR solution was increased, i.e., 67.23% for pH = 5 and 85.91% for pH = 3 were obtained (Table 6). However, lowering the pH to

Table 6. Degradation of $AR_{200\ ppm}$ by 0.020 g of MH20 after 60 min of Photocatalytic Activity at Various pH

pH	% AR degradation
3	85.91
5	67.23
7	50.32
9	39.08
11	25.33

a basic medium than neutral tends to decrease the % AR degradation. Degradation was reduced to 39.08% for pH = 9 and further decreased to 25.33% for pH = 11. Adsorption is maximum at acidic pH as the surface of the adsorbent becomes highly protonated and maximum adsorbate gets adsorbed on it by electrostatic forces of attraction whereas the adsorption rate becomes very low due to repulsive forces between adsorbent and adsorbate.

3.3. Kinetics and Mechanism of AR Degradation. Different kinetic models were applied to the experimental data obtained during photocatalytic $AR_{200\ ppm}$ degradation activity with **MH20** (0.020 g) at different time intervals. The pseudo-first-order ($\ln C_0/C_t$ vs t) kinetic model was found to be the best-fitted model on the obtained experimental data. The rate constant (k) for the AR degradation experiment was calculated through the linear equation and the R^2 value obtained close was close to 1 (Figure 8) indicating a significant correlation between experimental data obtained during photocatalytic activity with **MH20** with a rate constant of 0.9911.

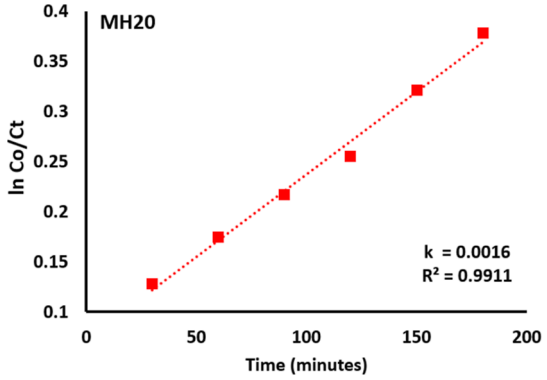

Figure 8. Pseudo-first-order kinetics of AR degradation by **MH20** (0.020 g).

We have earlier reported AR degradation mechanism over the surface of Cu-based manganese oxide catalysts.[21] The schematic illustration of degradation mechanism is shown in Figure 9. Upon absorption of light, the electrons (e^-) of the

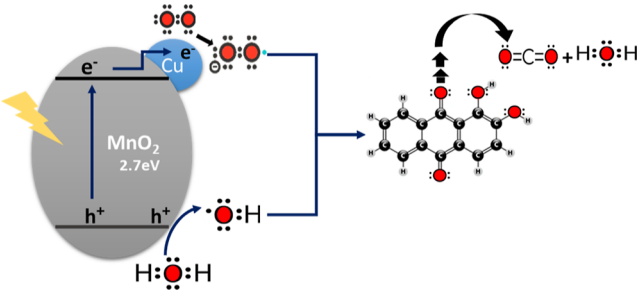

Figure 9. Schematic band diagram for AR degradation over Cu-based manganese oxide.

manganese oxide are excited from the valence band to the conduction band when UV light falls on the surface of the catalyst. This phenomenon results in generating the positive hole (h^+) in the valence band. The electron in the conduction band of MnO_2 will be picked up by the doped Cu nanoparticle as the work function of the metal is higher than that of metal oxide. A reactive superoxide anion radical ($^{\bullet}O^{2-}$) is generated by the uptake of electrons from metal nanoparticles by the adsorbed O_2 molecule present on the surface of the photocatalyst. Whereas, the positive holes present in the valence band react with H_2O molecules to form hydroxyl ($^{\bullet}OH$) radicals which are highly reactive toward the photo degradation of AR dye.[30] Hence, by tuning the structural parameters of these nanomaterials, their catalytic efficiencies can be enhanced enormously as can also be seen from the structural characterization of the catalysts.

https://doi.org/10.1021/acsomega.3c03736
ACS Omega 2023, 8, 35956−35963

4. CONCLUSIONS

The presented work described photocatalytic AR dye degradation by a series of Cu-based manganese oxide nanomaterials (**MH16−MH20**). Synthesized nanomaterials were successfully characterized by PXRD, SEM/EDX, BET, and PL techniques. Synthesized nanomaterials were analyzed to have a high mesoporous density as C constant values from BET were greater than 100, having a tetragonal crystalline system as per PXRD and exhibiting 2.98−3.02 eV band gap energies from the obtained UV−vis spectra and PL. **MH16−MH20** nanomaterials were utilized for photocatalytic AR dye degradation and under UV light % AR degradation was calculated at various time intervals from UV spectra. More than 60% AR degradation at various time intervals was obtained for **MH16−MH20** indicating their good catalytic efficiencies for AR removal. However, **MH20** was found to be the most efficient catalyst showing more than 84% degradation, hence **MH20** was used to investigate the effect of various catalytic doses, AR concentrations, and pH of the medium on degradation. More than 50% AR degradation was obtained for all studied parameters indicating good catalytic efficiency of **MH20**. The pseudo-first-order kinetic model was found to be the best-fitted kinetic model for AR degradation with k = 0.0015 and R^2 = 0.99 indicating a significant correlation between experimental data.

■ ASSOCIATED CONTENT

Supporting Information

The Supporting Information is available free of charge at https://pubs.acs.org/doi/10.1021/acsomega.3c03736.

SEM images of synthesized nanomaterials; N_2 adsorption−desorption isotherms of representative compound MH16; and absorption spectra of photocatalytic $AR_{200\ ppm}$ degradation activity at 30, 60, 90, 120, 150, and 180 min by 0.025 g of MH16−MH20 (PDF)

■ AUTHOR INFORMATION

Corresponding Author

Ataf Ali Altaf − *Department of Chemistry, University of Okara, Okara 56300, Pakistan; Department of Food Science, College of Agriculture and Life Sciences, Cornell University, Ithaca, New York 14853, United States;* orcid.org/0000-0001-8018-5890; Phone: +92-332-5049532; Email: atafali_altaf@yahoo.com

Authors

Muhammad Hamza − *Department of Chemistry, University of Gujrat, Gujrat 50700, Pakistan*

Samia Kausar − *Department of Chemistry, University of Gujrat, Gujrat 50700, Pakistan;* orcid.org/0000-0002-0219-2363

Shahzad Murtaza − *Institute of Chemistry, Khwaja Fareed UEIT, Rahim Yar Khan 64200, Pakistan*

Amen Shahpal − *Department of Chemistry and Catalysis Research Center, Technical University of Munich, Garching 85747, Germany*

Muhammad Hamayun − *Department of Chemistry, University of Gujrat, Gujrat 50700, Pakistan*

Muhammad Tayyab − *Key Laboratory for Advanced Materials and Institute of Fine Chemicals, School of Chemistry and Molecular Engineering, East China University of Science and Technology, Shanghai 200237, China*

Komal Rizwan − *Department of Chemistry, University of Sahiwal, Sahiwal 57000, Pakistan*

Hamza Shoukat − *Department of Chemistry, University of Gujrat, Gujrat 50700, Pakistan*

Anum Maqsood − *Department of Physics, The University of Lahore, Lahore 53700, Pakistan*

Complete contact information is available at: https://pubs.acs.org/10.1021/acsomega.3c03736

Author Contributions

Muhammad Hamza: conceptualization; investigation; methodology; and writing—original draft. Ataf Ali Altaf: conceptualization; formal analysis; supervision; and writing—review and editing. Samia Kausar: data curation; investigation; methodology; and writing—original draft. Shahzad Murtaza: formal analysis; supervision; and writing—review and editing. Amen Shahpal: data curation and resources. Muhammad Hamayun: resources and writing—review and editing. Muhammad Tayyab: resources. Komal Rizwan: resources and formal analysis. Hamza Shoukat: investigation and methodology. Anum Maqsood: resources.

Notes

The authors declare no competing financial interest.

■ REFERENCES

(1) (a) Tkaczyk, A.; Mitrowska, K.; Posyniak, A. Synthetic organic dyes as contaminants of the aquatic environment and their implications for ecosystems: A review. *Sci. Total Environ.* **2020**, *717*, 137222. (b) Naser, R.; Abu-Huwaij, R.; Al-khateeb, I.; Abbas, M. M.; Atoom, A. M. Green synthesis of zinc oxide nanoparticles using the root hair extract of Phoenix dactylifera: antimicrobial and anticancer activity. *Appl. Nanosci.* **2021**, *11*, 1747−1757. (c) Kansal, S. K.; Lamba, R.; Mehta, S.; Umar, A. Photocatalytic degradation of Alizarin Red S using simply synthesized ZnO nanoparticles. *Mater. Lett.* **2013**, *106*, 385−389.

(2) (a) Hussain, K. I.; Usman, M.; Siddiq, M.; Rasool, N.; Nazar, M. F.; Ahmad, I.; Holder, A. A.; Altaf, A. A. Application of micellar enhanced ultrafiltration for the removal of sunset yellow dye from aqueous media. *J. Dispersion Sci. Technol.* **2017**, *38*, 139−144. (b) Chung, K.-T. Azo dyes and human health: a review. *J. Environ. Sci. Health, Part C* **2016**, *34*, 233−261. (c) Sardar, M.; Manna, M.; Maharana, M.; Sen, S. Remediation of dyes from industrial wastewater using low-cost adsorbents. In *Green Adsorbents to Remove Metals, Dyes and Boron from Polluted Water*; Springer, 2021; pp 377−403.

(3) (a) Natarajan, S.; Bajaj, H. C.; Tayade, R. J. Recent advances based on the synergetic effect of adsorption for removal of dyes from waste water using photocatalytic process. *J. Environ. Sci.* **2018**, *65*, 201−222. (b) Oller, I.; Malato, S.; Sánchez-Pérez, J. Combination of advanced oxidation processes and biological treatments for wastewater decontamination—a review. *Sci. Total Environ.* **2011**, *409*, 4141−4166. (c) Li, Z.; Liu, J.; Zhang, F.-J.; Oh, W.-C. UV and visible light photodegradation effect on Fe−CNT/TiO 2 composite catalysts. *Bull. Mater. Sci.* **2013**, *36*, 293−299. (d) Akshatha, S.; Sreenivasa, S.; Parashuram, L.; Kumar, V. U.; Sharma, S.; Nagabhushana, H.; Kumar, S.; Maiyalagan, T. Synergistic effect of hybrid Ce3+/Ce4+ doped Bi2O3 nano-sphere photocatalyst for enhanced photocatalytic degradation of alizarin red S dye and its NUV excited photoluminescence studies. *J. Environ. Chem. Eng.* **2019**, *7*, 103053. (e) Chen, D.; Cheng, Y.; Zhou, N.; Chen, P.; Wang, Y.; Li, K.; Huo, S.; Cheng, P.; Peng, P.; Zhang, R.; et al. Photocatalytic degradation of organic pollutants using TiO2-based photocatalysts: A review. *J. Cleaner Prod.* **2020**, *268*, 121725. (f) Lellis, B.; Fávaro-Polonio, C. Z.; Pamphile, J. A.; Polonio, J. C. Effects of textile dyes on health and the environment and bioremediation potential of living organisms. *Biotechnol. Res. Innov.* **2019**, *3*, 275−290.

(4) Ali, H. Biodegradation of synthetic dyes—a review. *Water, Air, Soil Pollut.* **2010**, *213*, 251−273.
(5) Kumar, P. S.; Saravanan, A. Sustainable wastewater treatments in textile sector. In *Sustainable fibres and textiles*; Elsevier, 2017; pp 323−346.
(6) M'arimi, M.; Mecha, C.; Kiprop, A. K.; Ramkat, R. Recent trends in applications of advanced oxidation processes (AOPs) in bioenergy production: Review. *Renewable Sustainable Energy Rev.* **2020**, *121*, 109669.
(7) Panizza, M.; Oturan, M. A. Degradation of Alizarin Red by electro-Fenton process using a graphite-felt cathode. *Electrochim. Acta* **2011**, *56*, 7084−7087.
(8) (a) Verma, P.; Samanta, S. K. Microwave-enhanced advanced oxidation processes for the degradation of dyes in water. *Environ. Chem. Lett.* **2018**, *16*, 969−1007. (b) Machado, F. M.; Carmalin, S. A.; Lima, E. C.; Dias, S. L.; Prola, L. D.; Saucier, C.; Jauris, I. M.; Zanella, I.; Fagan, S. B. Adsorption of alizarin red S dye by carbon nanotubes: an experimental and theoretical investigation. *J. Phys. Chem. C* **2016**, *120*, 18296−18306. (c) Ghaedi, M.; Hassanzadeh, A.; Kokhdan, S. N. Multiwalled carbon nanotubes as adsorbents for the kinetic and equilibrium study of the removal of alizarin red S and morin. *J. Chem. Eng. Data* **2011**, *56*, 2511−2520.
(9) (a) Rani, M.; Shanker, U.; Chaurasia, A. K. Catalytic potential of laccase immobilized on transition metal oxides nanomaterials: degradation of alizarin red S dye. *J. Environ. Chem. Eng.* **2017**, *5*, 2730−2739. (b) Dong, H.; Zeng, G.; Tang, L.; Fan, C.; Zhang, C.; He, X.; He, Y. An overview on limitations of TiO2-based particles for photocatalytic degradation of organic pollutants and the corresponding countermeasures. *Water Res.* **2015**, *79*, 128−146. (c) Rauf, M.; Ashraf, S. S. Fundamental principles and application of heterogeneous photocatalytic degradation of dyes in solution. *Chem. Eng. J.* **2009**, *151*, 10−18.
(10) (a) Rauf, M.; Ashraf, S. S. Radiation induced degradation of dyes—an overview. *J. Hazard. Mater.* **2009**, *166*, 6−16. (b) Zhang, J.; Xiong, Z.; Zhao, X. Graphene−metal−oxide composites for the degradation of dyes under visible light irradiation. *J. Mater. Chem.* **2011**, *21*, 3634−3640. (c) Ling, S. K.; Wang, S.; Peng, Y. Oxidative degradation of dyes in water using Co2+/H2O2 and Co2+/peroxymonosulfate. *J. Hazard. Mater.* **2010**, *178*, 385−389.
(11) Sood, S.; Mehta, S. K.; Umar, A.; Kansal, S. K. The visible light-driven photocatalytic degradation of Alizarin red S using Bi-doped TiO 2 nanoparticles. *New J. Chem.* **2014**, *38*, 3127−3136.
(12) Sun, J.; Lu, H.; Du, L.; Lin, H.; Li, H. Anodic oxidation of anthraquinone dye Alizarin Red S at Ti/BDD electrodes. *J. Hazard. Mater.* **2011**, *257*, 6667−6671.
(13) Joshi, K.; Shrivastava, V. Degradation of alizarine red-S (A textiles dye) by photocatalysis using ZnO and TiO2 as photocatalyst. *Int. J. Environ. Sci.* **2011**, *2*, 8−21.
(14) Karimi-Maleh, H.; Kumar, B. G.; Rajendran, S.; Qin, J.; Vadivel, S.; Durgalakshmi, D.; Gracia, F.; Soto-Moscoso, M.; Orooji, Y.; Karimi, F. Tuning of metal oxides photocatalytic performance using Ag nanoparticles integration. *J. Mol. Liq.* **2020**, *314*, 113588.
(15) Jabeen, U.; Shah, S. M.; Khan, S. U. Photo catalytic degradation of Alizarin red S using ZnS and cadmium doped ZnS nanoparticles under unfiltered sunlight. *Surf. Interfaces* **2017**, *6*, 40−49.
(16) Rao, Y.; Zhang, Y.; Li, A.; Zhang, T.; Jiao, T. Photocatalytic activity of G-TiO2@ Fe3O4 with persulfate for degradation of alizarin red S under visible light. *Chemosphere* **2021**, *266*, 129236.
(17) Altaf, A. A.; Ahmed, M.; Hamayun, M.; Kausar, S.; Waqar, M.; Badshah, A. Titania nano-fibers: a review on synthesis and utilities. *Inorg. Chim. Acta* **2020**, *501*, 119268.
(18) Duan, J.; Zheng, Y.; Chen, S.; Tang, Y.; Jaroniec, M.; Qiao, S. Mesoporous hybrid material composed of Mn3O4 nanoparticles on nitrogen-doped graphene for highly efficient oxygen reduction reaction. *Chem. Commun.* **2013**, *49*, 7705−7707.
(19) (a) Kausar, S.; Altaf, A. A.; Hamayun, M.; Rasool, N.; Hadait, M.; Akhtar, A.; Muhammad, S.; Badshah, A.; Shah, S. A. A.; Zakaria, Z. A. i-Propylammonium Lead Chloride Based Perovskite Photocatalysts for Depolymerization of Lignin Under UV Light. *Molecules* **2020**, *25*, 3520. (b) Kausar, S.; Ali Altaf, A.; Hamayun, M.; Danish, M.; Zubair, M.; Naz, S.; Muhammad, S.; Zaheer, M.; Ullah, S.; Badshah, A. Soft template-based bismuth doped zinc oxide nanocomposites for photocatalytic depolymerization of lignin. *Inorg. Chim. Acta* **2020**, *502*, 119390.
(20) Kansal, S.; Singh, M.; Sud, D. Studies on TiO2/ZnO photocatalysed degradation of lignin. *J. Hazard. Mater.* **2008**, *153*, 412−417.
(21) Hamza, M.; Altaf, A. A.; Kausar, S.; Murtaza, S.; Rasool, N.; Gul, R.; Badshah, A.; Zaheer, M.; Ali Shah, S. A.; Zakaria, Z. A. Catalytic removal of alizarin red using chromium manganese oxide nanorods: degradation and kinetic studies. *Catalysts* **2020**, *10*, 1150.
(22) Cai, X.; Zhao, S.; Cai, D.; Zheng, J.; Zhu, Z.; Wei, D.; Zheng, Z.; Zhu, H.; Chen, Y. Synthesis and evaluation of novel D-ring substituted steroidal pyrazolines as potential anti-inflammatory agents. *Steroids* **2019**, *146*, 70−78.
(23) Cullity, B.; Stock, S. *Elements of X-ray Diffraction*, 3rd ed.; Prentice Hall: New York, 2001; pp 174−177.
(24) Aé, L.; Kieven, D.; Chen, J.; Klenk, R.; Rissom, T.; Tang, Y.; Lux-Steiner, M. C. ZnO nanorod arrays as an antireflective coating for Cu (In, Ga) Se2 thin film solar cells. *Prog. Photovolt.* **2010**, *18*, 209−213.
(25) Shoukat, H.; Altaf, A. A.; Hamayun, M.; Ullah, S.; Kausar, S.; Hamza, M.; Muhammad, S.; Badshah, A.; Rasool, N.; Imran, M. Catalytic Oxidation of Toluene into Benzaldehyde and Benzyl Alcohol Using Molybdenum-Incorporated Manganese Oxide Nanomaterials. *ACS Omega* **2021**, *6*, 19606−19615.
(26) Bindu, P.; Thomas, S. Estimation of lattice strain in ZnO nanoparticles: X-ray peak profile analysis. *J. Theor. Appl. Phys.* **2014**, *8*, 123−134.
(27) Sarkar, P.; Mazumder, J.; Tripathy, S.; Baishnab, K.; Palai, G. Structural, optoelectronic, and morphological study of indium-doped methylammonium lead chloride perovskites. *Appl. Phys. A* **2019**, *125*, 580.
(28) (a) De Matteis, F.; Vitale, F.; Privitera, S.; Ciotta, E.; Pizzoferrato, R.; Generosi, A.; Paci, B.; Di Mario, L.; Pelli Cresi, J. S.; Martelli, F.; et al. Optical Characterization of Cesium Lead Bromide Perovskites. *Crystals* **2019**, *9*, 280. (b) Labhsetwar, N. K.; Watanabe, A.; Mitsuhashi, T. New improved syntheses of LaRuO3 perovskites and their applications in environmental catalysis. *Appl. Catal., B* **2003**, *40*, 21−30. (c) Zhu, J.; Li, H.; Zhong, L.; Xiao, P.; Xu, X.; Yang, X.; Zhao, Z.; Li, J. Perovskite oxides: preparation, characterizations, and applications in heterogeneous catalysis. *ACS Catal.* **2014**, *4*, 2917−2940.
(29) (a) Mondal, D.; Das, S.; Paul, B. K.; Bhattacharya, D.; Ghoshal, D.; Gayen, A. L.; Das, K.; Das, S. Size engineered Cu-doped α-MnO2 nanoparticles for exaggerated photocatalytic activity and energy storage application. *Mater. Res. Bull.* **2019**, *115*, 159−169. (b) Janani, B.; Syed, A.; Hari Kumar, B.; Elgorban, A. M.; Bahkali, A. H.; Ahmed, B.; Das, A.; Sudheer Khan, S. High performance MnO2−Al2O3 nanocomposite as white light photocatalyst and bactericidal agent: Insights on photoluminescence and intrinsic mechanism. *Opt. Mater.* **2021**, *120*, 111438. (c) Yu, T.; Sun, Y.; Zhe, C.; Wang, W.; Rao, P. Synthesis of CuO x/MnO 2 Heterostructures with Enhanced Visible Light-Driven Photocatalytic Activity. *J. Mater. Sci. Chem. Eng.* **2017**, *05*, 12−25.
(30) Xue, J.; Chen, L.; Wang, H. Degradation mechanism of Alizarin Red in hybrid gas−liquid phase dielectric barrier discharge plasmas: experimental and theoretical examination. *Chem. Eng. J.* **2008**, *138*, 120−127.

https://doi.org/10.1021/acsomega.3c03736
ACS Omega 2023, 8, 35956−35963